



Science Arts & Métiers (SAM)

is an open access repository that collects the work of Arts et Métiers Institute of Technology researchers and makes it freely available over the web where possible.

This is an author-deposited version published in: <https://sam.ensam.eu>
Handle ID: [.http://hdl.handle.net/10985/21500](http://hdl.handle.net/10985/21500)

To cite this version :

Abderezak AOUALI, Stéphane CHEVALIER, Alain SOMMIER, M. AYADI, Jean-Christophe BATSALE, Daniel BALAGEAS, Christophe PRADERE - Ultra-broadband contactless imaging power meter - Applied Optics - Vol. 60, n°26, p.7995 - 2021

Any correspondence concerning this service should be sent to the repository

Administrator : scienceouverte@ensam.eu



Ultra-broadband contactless imaging power meter

A. AOUALI,^{1,*} S. CHEVALIER,² A. SOMMIER,¹ M. AYADI,² J.-C. BATSALE,² D. BALAGEAS,¹ AND C. PRADERE¹

¹I2M TREFLE, UMR 5295 CNRS-UB-ENSAM, 351 Cours de la Libération, 33400 Talence, France

²Arts et Métiers Institute of Technology, Université de Bordeaux, CNRS, INRA, INP, I2M, HESAM. Esplanade des arts et métiers, F-33400 Talence, France

*Corresponding author: abderezak.aouali@u-bordeaux.fr

Received 1 June 2021; revised 30 July 2021; accepted 4 August 2021; posted 6 August 2021 (Doc. ID 432479); published 0 MONTH 0000

Knowledge of the spatial and temporal distribution of heat flux is of great interest for the quantification of heat sources. In this work, we describe the development of a new ultra-broadband contactless imaging power meter based on electromagnetic to infrared technology. This new sensor and the mathematical processing of images enable the reconstruction of both spatial and amplitude distributions through a wide spectral range of sources. The full modeling of the thermoconverter based on 3D formalism of thermal quadrupoles is presented first before deriving a reduced model more suitable for quick and robust inverse processing. The inverse method makes it possible to simultaneously identify the heat losses and the spatial and temporal source distribution for the first time, to the best of our knowledge. Finally, measurements of multispectral sources are presented and discussed, with an emphasis on the spatial and temporal resolution, accuracy and capabilities of the power meter. © 2021 Optical Society of America

<https://doi.org/10.1364/AO.432479>

Nomenclature

A	Absorbance
T	Temperature in real space, K
$\hat{\theta}$	Temperature in the cosine transformed space
θ	Temperature in cosine and Laplace transformed space
h_c	Convective exchange coefficient, $\text{W m}^{-2} \text{K}^{-1}$
\hat{h}	Source point impulse response in real space
H	Source point impulse response in cosine and Laplace transformed space
\hat{H}	Source point impulse response in cosine transformed space
\hat{H}^\ominus	Source point Heaviside response in cosine transformed space
\mathcal{Y}	Internal source in real space, W m^{-3}
Y	Internal source in cosine and Laplace transformed space
δ	Dirac function
Θ	Heaviside function
λ	Thermal conductivity, $\text{W m}^{-1} \text{K}^{-1}$
a	Thermal diffusivity, $\text{m}^2 \text{s}^{-1}$
ρ	Mass density, kg m^{-3}
C_p	Specific heat, $\text{J K}^{-1} \text{kg}^{-1}$
ϕ_0, ϕ_e	Excitation flux in boundary condition (respectively, input and output fluxes), W m^{-2}
e	Thickness of the thermoconverter, m

L	Lateral dimension of the thermoconverter, m
t	Time, s
x, y, z	Spatial coordinates
Z_j^i	Thermal impedance in Laplace and cosine transform space, i
layer number, j	Thermal impedance number
∇	Laplacian

1. INTRODUCTION

The development of imaging sensors to measure radiative heat flux has attracted a considerable amount of attention in the research community in recent years. Whereas many works have focused on imaging sensors for visible light [1–4], few tools exist for other wavelength ranges, particularly the millimeter to meter range [5,6]. Knowledge of the heat flux generated by a multispectral source is of prime interest in numerous experimental setups, i.e., in building sciences, aeronautic industries, optical applications, and heat transfer. A quantitative image of radiative heat flux (or thermal source) would enable the performance of heat balance to serve as input data for models or to control online processes. In this context, the development of a new sensor implies, first, developing the hardware (the component sensitive to the heat excitation) and, second, determining the

(Table continued)

36 mathematical modeling of the hardware response to obtain
37 quantitative data.

38 There are two main types of flux sensors: thermal and pho-
39 tonic sensors. Photonic sensors are based on the photoelectric
40 effect and are predominantly used at higher frequencies in the
41 visible, ultraviolet, and X-ray spectral ranges [7]. In contrast,
42 thermal detectors are mainly used at longer wavelengths [5,6].
43 In this study, the choice of hardware is based on the electro-
44 magnetic infrared (EMIR) technology developed by Balageas
45 *et al.* [8]. In their work, Balageas *et al.* reported a hyperspectral
46 sensor using a very thin and homogeneous carbon film called
47 a hyperspectral thermoconverter. This device has the ability to
48 absorb radiation over a very wide spectral range (from visible
49 to radio waves) with different sensitivities (depending on the
50 wavelength) [5,9]. Electromagnetic waves are absorbed by the
51 carbon film and converted into heat, which is transported by
52 conduction in the thin film before being re-emitted as infrared
53 (IR) light. Thus, this carbon thermoconverter enables imaging
54 of ultra-broadband heat flux when used in combination with
55 an IR camera. However, before obtaining a quantitative image
56 of the heat flux or the thermal source detected by the sensor,
57 thorough mathematical processing based on thermal inverse
58 methods is required.

59 Depending on the nature of the heat transfer, i.e., conduc-
60 tion, convection, or radiation, there are several methods for
61 estimating the heat source [10–12]. In the present study, the
62 reconstruction of the heat fields is essentially based on the
63 knowledge of conductive transfer. Garderein *et al.* [13] devel-
64 oped a point sensor system based on a thermocouple to estimate
65 local fluxes by analytical inverse thermal methods. Another
66 study from Zeribi *et al.* [14] reported the fabrication of a 2D
67 non-imaging heat flux sensor based on the spatial temperature
68 gradient method. Image reconstruction was addressed by Groz
69 *et al.* [15,16], who reported a method to reconstruct deep heat
70 sources using analytical models and two inversion methods
71 (statistical and deconvolution by Toeplitz). Another 3D recon-
72 struction method was recently developed by Burgholzer *et al.*
73 [17,18]. This method combines IR thermography and the con-
74 cept of virtual waves. However, in these studies, the quantitative
75 goal of estimating the heat flux amplitude was not achieved
76 because the location of the sources is assumed to be unknown.
77 Finally, Nortershauser *et al.* [19,20] addressed the development
78 of a source reconstruction method (spatial distribution and flux
79 amplitude) using numerical models for inversion. The con-
80 straint of this method is mainly related to the calculation time.
81 However, the authors proposed the use of a statistical estimator
82 in the cosine transformed space to reduce the calculation time.

83 From all of these seminal works, it was demonstrated that both
84 quantitation and spatial distribution of the heat flux are needed
85 to process the images formed on a thermal thermoconverter.
86 Such a quantitative method combined with the EMIR technol-
87 ogy will enable the development of new electromagnetic sensors
88 to reconstruct both spatial and amplitude distributions over
89 a wide spectral range by passing through cosine transformed
90 space. Indeed, this passage through cosine transformed space is
91 of considerable interest when calculating convolution products
92 and results in a substantial advantage in terms of calculation
93 time.

94 The present work reports the development of an ultra-
95 broadband contactless imaging power meter. To the best of our
96 knowledge, such a hyperspectral sensor allowing the measure-
97 ment of thermal flux images and the reconstruction of the source
98 has not previously been reported in the literature. To address
99 this objective, the thermophysical properties of the hardware,
100 i.e., the thermoconverter associated with a research-grade IR
101 camera, are thoroughly characterized. The method used for
102 mathematical processing of the images formed on the thermo-
103 converter is then presented. Finally, several examples at various
104 wavelengths [from near-IR (NIR) to radio waves] are presented
105 and discussed. The limits and accuracy of these new sensors are
106 also discussed at the end of the paper.

2. EXPERIMENTAL SETUP

107 The experimental setup is described in a general manner in
108 Fig. 1. A multispectral source is used to optically illuminate
109 and heat the thermoconverter by the photothermal effect.
110 The heat absorption depends on the wavelength. For example,
111 the absorbance is 100% in the NIR to far-IR range and only
112 61% in the millimeter range [9]. Heating the film increases its
113 thermal radiative emission, which is detected by an IR camera.
114 The camera used is an InSb SC 7000 from FLIR [working in
115 the spectral range (1.5–5.5 μm) with 240×320 pixels and a
116 pitch size of $25 \mu\text{m} \times 25 \mu\text{m}$, this camera will be used for all
117 powermeter applications] placed behind the thermoconverter
118 (in this IR band, the thermoconverter can be assimilated to a
119 blackbody $\epsilon \approx 1$ [9]). This photon-phonon-photon conversion
120 has the advantage of being ultra-broadband and the drawback
121 of not having enough power to sufficiently heat the converter to
122 achieve acceptable IR camera sensitivity.
123

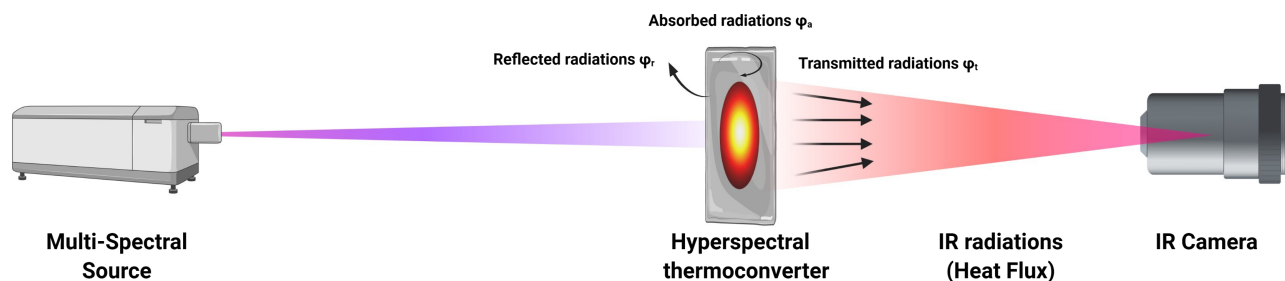


Fig. 1. Schema of the experimental setup.

124
125
126
127
128
129
130
131
132
133
134
135
136
137
138
139
140
141
142
143
144
145

3. MODELING HEAT TRANSFER IN THE THERMOCONVERTER

A. Complete Thermal Model of the Thermoconverter

The thermoconverter can be considered a thin homogeneous medium (a thermally thin body due to its small thickness, $L = 5$ cm and $e = 37 \mu\text{m}$) subjected to convective/radiative heat loss and containing an internal heat source. Due to the very large ratio between the lateral dimensions and the thickness ($L \gg e$), the temperature gradient across the thickness of the thermoconverter is neglected. Thus, it is advisable to consider the surrounding environment [21]. The influence of the air around the thermoconverter is not negligible and considerably affects the temperature of the thermoconverter. This can be explained by the presence of effusive exchanges between the thermoconverter (thermally thin body) and the surrounding environment. Therefore, the analytical model that accurately describes the heat transfer in the thermoconverter must include the surrounding layers. In Fig. 2, there are three layers: air-thermoconverter-air. The evolution of the temperature fields in the system described in Fig. 2 is determined by the three-layer 3D heat conduction equation with an internal volume source located in the thermoconverter layer:

$$\left\{ \begin{array}{l} \frac{1}{a_r} \frac{\partial T_r(x, y, z, t)}{\partial t} - \frac{1}{\lambda_{r=2}} \mathcal{D}_{r=2}(x, y, z, t) - \nabla^2 T_r(x, y, z, t) = 0, \quad r = 1, 2, 3, \\ -\lambda_r \frac{\partial T_r(x, y, z, t)}{\partial x} \Big|_{x=\pm \frac{L_x}{2}} = 0, \quad -\lambda_r \frac{\partial T_r(x, y, z, t)}{\partial y} \Big|_{y=\pm \frac{L_y}{2}} = 0, \\ \lambda_{r=1} \frac{\partial T_{r=1}(x, y, z, t)}{\partial z} \Big|_{z=j} = -\lambda_{r=2} \frac{\partial T_{r=2}(x, y, z, t)}{\partial z} \Big|_{z=j} = -h_c T_{r=2}(x, y, z = j, t), \\ -\lambda_{r=2} \frac{\partial T_{r=2}(x, y, z, t)}{\partial z} \Big|_{z=k} = \lambda_{r=3} \frac{\partial T_{r=3}(x, y, z, t)}{\partial z} \Big|_{z=k} = h_c T_{r=2}(x, y, z = k, t), \\ T_{r=1}(x, y, z = j, t) = T_{r=2}(x, y, z = j, t), \\ T_{r=2}(x, y, z = k, t) = T_{r=3}(x, y, z = k, t), \\ T_r(x, y, z, t = 0) = 0, \end{array} \right. \quad (1)$$

146
147

where r is the layer number, i.e., 1 for air, 2 for the thermoconverter, and 3 for air, as depicted in Fig. 2.

148

B. Assumptions and Solution

149
150
151

In this part, the solution of the three-layer system is described. This solution is based on the 3D formalism of thermal quadrupoles [22,23] using the transformed impedances in

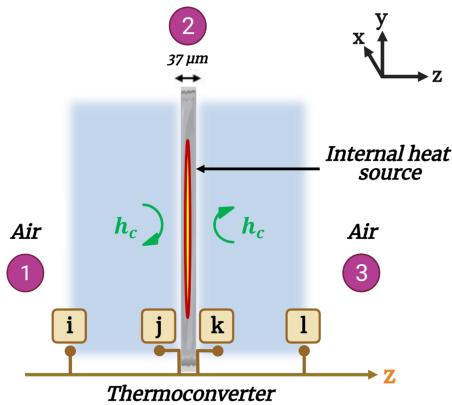


Fig. 2. Complete thermal model of the thermoconverter (i, l, physical boundary of the air layers; j, k, plans of the interfaces between the thermoconverter and the air layers).

cosine Laplace spaces. The equivalent electrical network of the system is shown in Fig. 3(a), in which each layer is composed of three impedances. In this case, it is considered that the contact between the layers is perfect (no contact thermal resistance between the layers), and the internal source is uniformly distributed through the entire thickness of the thermoconverter. To solve the three-layer system, the following assumptions are made:

- Adiabatic boundary conditions on each side of layers 1 and 3: the impedances Z_1^1 of layer 1 and Z_2^3 of layer 3 are neglected [Fig. 3(b)] because the interest is focused only on the energy contribution of the internal heat source, as shown in Fig. 2 (absence of ϕ_0 and ϕ_e).
- Semi-infinite medium configuration: the purpose of choosing a three-layer system as a model is to take into account the influences of adjacent media (mainly air) on the thermoconverter, so the impedances Z_3^3 and Z_2^1 of layer 1 and the impedances Z_1^3 and Z_3^3 of layer 3 are replaced by two semi-infinite impedances, Z_∞^1 and Z_∞^3 , respectively [Fig. 3(c)].
- Thermally thin body: the thermoconverter was previously described as a thermally thin body (no temperature gradient in

152
153
154
155
156
157
158
159
160
161
162
163
164
165
166
167
168
169
170
171
172
173
174

146
147

the thickness). This leads to the suppression of the impedances Z_1^{th} and Z_2^{th} , and only the impedance Z_3^{th} is necessary to evaluate the temperature of the thermoconverter [Fig. 3(d)].

148

Figure 3 shows the reduction steps according to the assumptions made, as well as the equivalent electrical networks obtained at each step. Based on the electric current conservation law at the node of the thermoconverter layer in Fig. 3(d), the temperature expression of the thermoconverter in the Laplace cosine transformed space is written as follows:

$$\theta_{\text{Th}} = \left(\frac{1}{Z_{\text{eq}}^1} + \frac{1}{Z_{\text{Th}}^3} + \frac{1}{Z_{\text{eq}}^3} \right)^{-1} \times Y, \quad (2)$$

with

$$Z_{\text{eq}}^{1,3} = \left(b + \frac{1}{Z_\infty^{1,3}} \right)^{-1}, \quad \text{where } Z_\infty^{1,3} = (\lambda\gamma)^{-1} \quad \text{and} \quad \gamma = \sqrt{\frac{p}{a} + \alpha_n^2 + \beta_m^2}. \quad (3)$$

The capacitive impedance of the thermoconverter is written as follows:

175
176
177
178
179
180
181
182
183
184

185

186
187

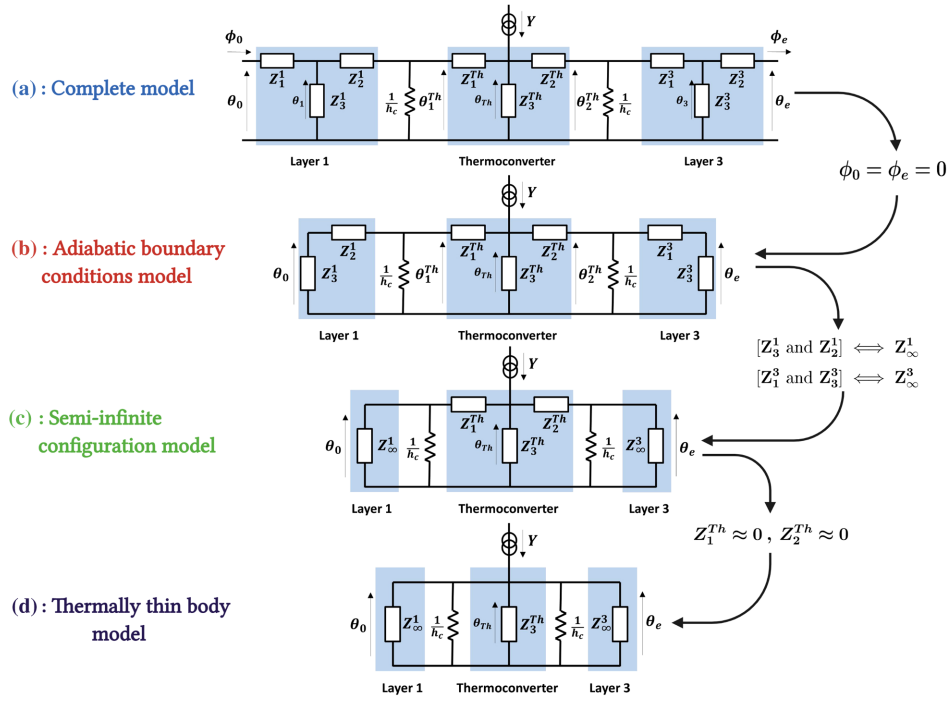


Fig. 3. Reduction steps of the thermoconverter model: (a) complete model, (b) adiabatic boundary conditions model, (c) semi-infinite configuration model, and (d) thermally thin body model.

$$Z_3^{Th} = (\lambda \gamma \sinh(\gamma \ell))^{-1}, \quad \text{where } \gamma = \sqrt{\frac{p}{a} + \alpha_n^2 + \beta_m^2}, \quad (4)$$

where $\alpha_n = n\pi/L_x$, $n \in \mathbb{N}$ and $\beta_m = m\pi/L_y$, $m \in \mathbb{N}$ represent the spatial frequencies, and p represents the Laplace variable. Y represents the internal source in Laplace cosine transformed space, it is written as

$$Y(\alpha_n, \beta_m, p) = \int_0^{+\infty} \int_0^{L_x} \int_0^{L_y} \mathcal{Y}(x, y, t) \times \exp(-pt) \cos(\alpha_n x) \cos(\beta_m y) dt dx dy. \quad (5)$$

Finally, the temperature of the thermoconverter in the Laplace cosine transformed space is obtained as

$$\theta_{Th}(\alpha_n, \beta_m, p) = \int_0^{+\infty} \int_0^{L_x} \int_0^{L_y} T_{Th}(x, y, t) \times \exp(-pt) \cos(\alpha_n x) \cos(\beta_m y) dt dx dy. \quad (6)$$

Equation (2) can be rewritten simply as follows:

$$\theta_{Th}(\alpha_n, \beta_m, p) = H(\alpha_n, \beta_m, p) \times Y(\alpha_n, \beta_m, p),$$

$$H(\alpha_n, \beta_m, p) = \left(\frac{1}{Z_{eq}^1} + \frac{1}{Z_3^{Th}} + \frac{1}{Z_{eq}^3} \right)^{-1}. \quad (7)$$

To compute the spatial temperature field, one inverse Laplace in time [24] and two inverse cosine transformations are necessary.

Table 1. Thermophysical Properties of the Different Layers Given in Ref. [26] for Air

	Air	Thermoconverter
Thickness (m)	∞	$37 \pm 1 \times 10^{-6}$
λ ($\text{W m}^{-1} \text{K}^{-1}$)	0.026	1.414 ± 0.041
ρC_p ($\text{J K}^{-1} \text{m}^{-3}$)	1313	$2.83 \pm 0.03 \times 10^6$
a ($\text{m}^2 \text{s}^{-1}$)	1.98×10^{-5}	$5.0 \pm 0.1 \times 10^{-7}$

All of the parameters of the thermoconverter needed for the construction of the model have been estimated. The thickness measured by a micrometer was $37 \pm 1 \mu\text{m}$. The thermal diffusivity was estimated by the flying spot technique [25] to be $a = 5.0 \pm 0.1 \times 10^{-7} \text{m}^2 \cdot \text{s}^{-1}$. Using conventional thermal characterization techniques, the remaining thermophysical properties of the thermoconverter were measured: (i) the density was calculated by means of a helium pycnometer to be $\rho = 1800 \pm 10 \text{kg} \cdot \text{m}^{-3}$, and (ii) the specific heat was estimated by a Setaram 131 differential scanning calorimeter to be $C_p = 1572 \pm 8 \text{J} \cdot \text{K}^{-1} \cdot \text{kg}^{-1}$.

The thermophysical properties of air were obtained from the literature [26] (see Table 1).

C. Validation of the Assumptions

Two studies have been carried out, as described in this section, to validate the assumptions made previously. The first study consists of a comparison between the temperature fields of the thermoconverter calculated by means of the four different models described in Fig. 3. The spatial shape of the source used is concentric circles, and a Dirac pulse $\delta(t)$ was used for temporal excitation. The value of the heat loss was set to

198
199
200
201
202
203
204
205
206
207
208
209
210

211
212
213
214
215
216
217
218

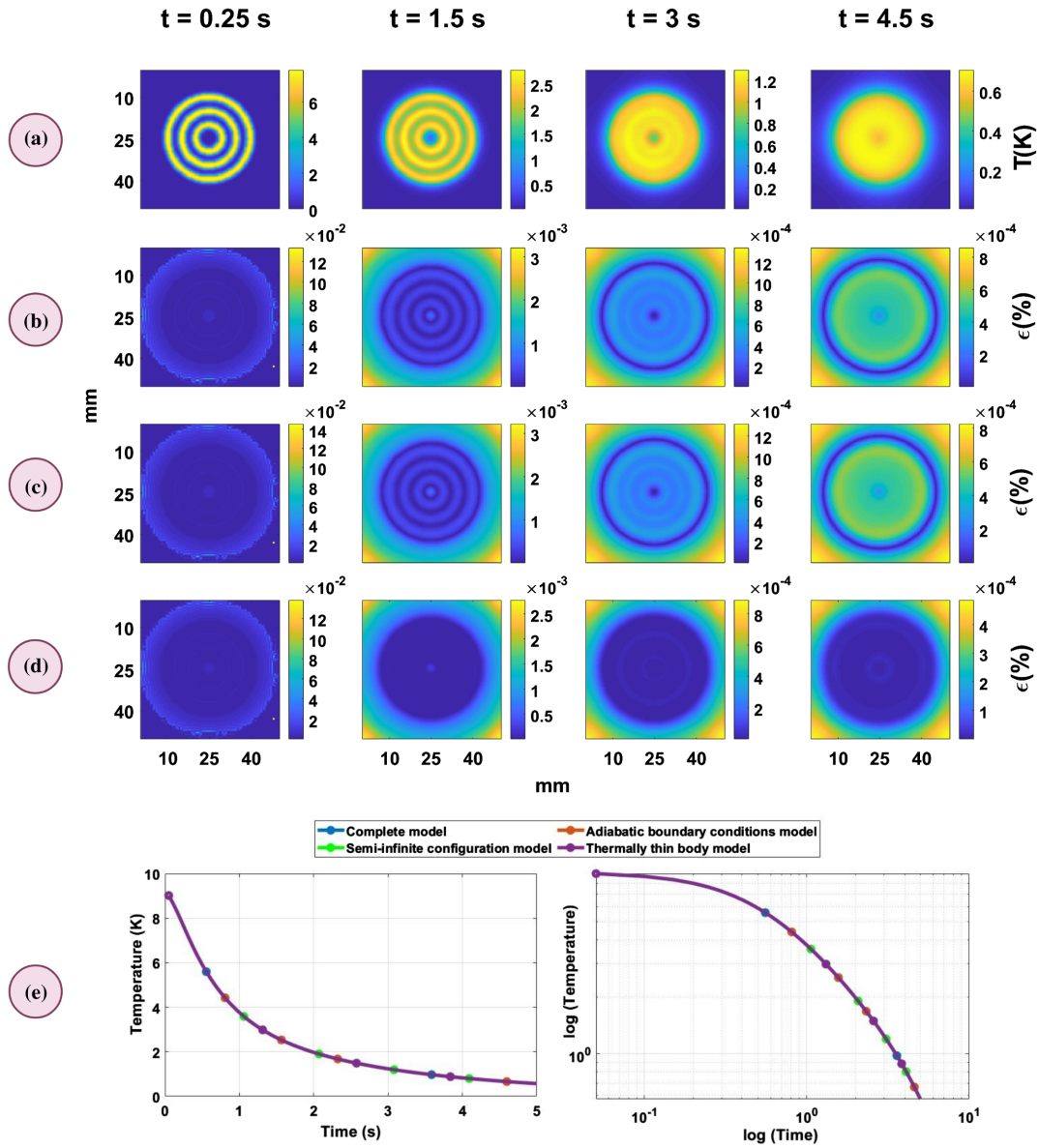


Fig. 4. Comparison of the temperature determined by the four models: (a) diffusion of the source obtained by the complete model, (b) calculated error (in %) between the source diffusion obtained from the complete model and that obtained from the adiabatic boundary conditions model, (c) calculated error (in %) between the source diffusion obtained from the complete model and that obtained from the semi-infinite configuration model, (d) calculated error (in %) between the source diffusion obtained from the complete model and that obtained from the thermally thin body model, and (e) diffusion of one pixel versus time determined by the four models.

219 $h_c = 20 \text{ W} \cdot \text{m}^{-2} \cdot \text{K}^{-1}$. This study allows the validation of
 220 the reduction steps of the model. The second study consists
 221 of generating a flux balance using the model to calculate the
 222 rate of heat flux dissipated in each impedance that constitutes
 223 the system. This second study allows quantitative evaluation
 224 of the heat transfer mechanism contribution and the effect of
 225 considering the air layers in the model.

226 It can be seen from Fig. 4 that the temperature fields of the
 227 thermoconverter are quasi-identical for the four different mod-
 228 els. Figure 4(e) confirms the previous finding by showing that
 229 the transient heat transport is also identical for the different
 230 models. This effectively enables the validation the different
 231 assumptions described in Section 3.B.

232 Figure 5 illustrates the flux balance. Figure 5(a) shows the rate
 233 of the transient heat flux (delivered by the internal source) dissi-
 234 pated by the volume of the thermoconverter, air, and convective
 235 heat loss. Figure 5(b) shows the sum of all of the fluxes, which
 236 must be equal to 100% at all times (conservation of energy). In
 237 Fig. 5(a), we can see that at short times ($t < 2$ s) the influence
 238 of the air layers appears very early and is important enough to
 239 be neglected (5% at $t = 0.17$ s, 10% at $t = 0.8$ s). Moreover,
 240 the heat flux dissipated by convective heat loss intervenes later
 241 than the air (5% at $t = 1$ s, 10% at $t = 2$ s) to then reach a more
 242 important rate at long times (35% at $t = 10$ s). In conclu-
 243 sion, it should be noted that the dissipation of the flux in the
 244 semi-infinite impedances of the air occurs rapidly and is quite

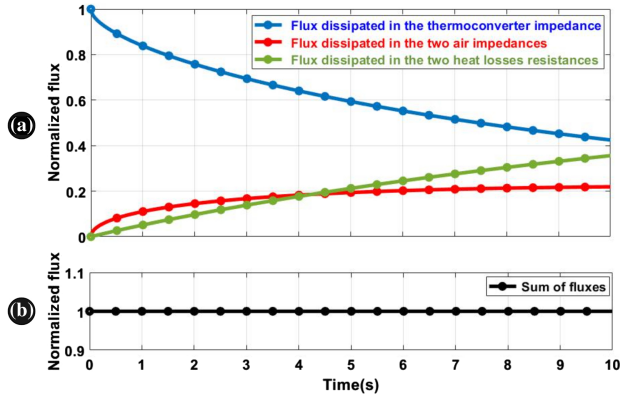


Fig. 5. Heat flux balance.

important. This proves that the consideration of the environment around the thermoconverter in the model is primordial. It should also be noted that the dissipation of the flux through the heat loss resistances occurs less rapidly over time and is also important. Therefore, it is necessary to estimate the heat losses to form a complete model.

4. INVERSE METHOD DESCRIPTION

A. Inverse Method for Source Estimation

Based on Eq. (7), the output temperature can simply be written as a space–time convolution product of the source and the impulse response of the source point:

$$T_{\text{Th}}(x, y, t) = \mathcal{Y}(x, y, t) \otimes \hat{h}(x, y, t), \quad (8)$$

where $\hat{h}(x, y, t)$ is the impulse response in real space–time. The source $\mathcal{Y}(x, y, t)$ can be decomposed into a product of a spatial function $\mathcal{F}(x, y)$, amplitude \mathcal{Y}_0 , and a temporal function $\Theta(t)$. After passing through the space transformed cosine base, only the temporal convolution remains. In the case of a Heaviside-type temporal excitation and after applying the Laplace transform on time, we have

$$\theta_{\text{Th}}(\alpha_n, \beta_m, p) = \mathcal{Y}_0 \times \hat{\mathcal{F}}(\alpha_n, \beta_m) \times \underbrace{\left[\frac{1}{p} \times H(\alpha_n, \beta_m, p) \right]}_{H^\ominus}, \quad (9)$$

where H^\ominus represents the response of the source point to the Heaviside temporal excitation in Laplace cosine transformed space. By applying the Laplace inverse transform to Eq. (9), the source can be estimated in the cosine transformed space via the following relation:

$$\mathcal{Y}_0 \times \hat{\mathcal{F}}(\alpha_n, \beta_m) = \hat{\theta}_{\text{Th}}(\alpha_n, \beta_m, t) \times \left[\hat{H}^\ominus(\alpha_n, \beta_m, t) \right]^{-1}. \quad (10)$$

Inverse thermal problems are known to be ill-posed problems [27]. This is essentially due to the condition of instability of the solution obtained by inversion. To remedy this condition, the inversion is carried out by constructing a Wiener filter. This filter is based on Tikhonov’s regularization method [28], which is used and applied in the Cosine transformed space as follows:

$$\mathcal{Y}_0 \times \hat{\mathcal{F}}(\alpha_n, \beta_m) = \hat{\theta}_{\text{Th}}(\alpha_n, \beta_m, t) \times \frac{\hat{H}^\ominus(\alpha_n, \beta_m, t)}{|\hat{H}^\ominus(\alpha_n, \beta_m, t)|^2 + \mu |\hat{D}(\alpha_n, \beta_m)|^2}, \quad (11)$$

where D is a derivation matrix [29] in the cosine transformed space, and μ is the regularization coefficient [30]. In the end, to retrieve the spatial distribution of the source, two inverse cosine transformations are necessary.

B. Heat Losses Estimation

As shown in Section 3.C, the heat losses by convection need to be measured along with the spatial distribution of the source in order to adapt to the external environment. Thus, based on the fact that the spatial average of a 3D temperature field leads to the one-dimensional (1D) temperature field [22] and the fact that the relaxation of the temperature field due to a Heaviside excitation corresponds to a response to an amplified Dirac excitation, a method of heat loss estimation based on a linear least-squares minimization between the normalized spatial average of the relaxation experimental temperature field (see Fig. 6) and the normalized spatial average of temperature field obtained from the model Eq. (2) (for a Dirac time excitation) is described in this section.

Assuming that the measured temperature field of the thermoconverter is $T_{\text{mes}}(x, y, t)$, the spatial average of this temperature field is calculated for each time step and normalized by its maximum to arrive at $\tilde{T}_{\text{mes}}^*(t)$.

Then, a variable change over time is applied, $t^* = t - t_0$, where t_0 corresponds to the time of the beginning of relaxation ($\tilde{T}_{\text{mes}}^*(t_0) = 1$); this new time base t^* is used to calculate the numerical temperature field of the thermoconverter (for a Dirac time excitation) from the model described in Section 3.B for different values of h_c . The temperature field obtained is spatially averaged and then normalized by its maximum to obtain the following: $\tilde{T}_{\text{model}}^*(t^*)$.

Finally, the minimization is achieved using the Nelder–Mead simplex method [31],

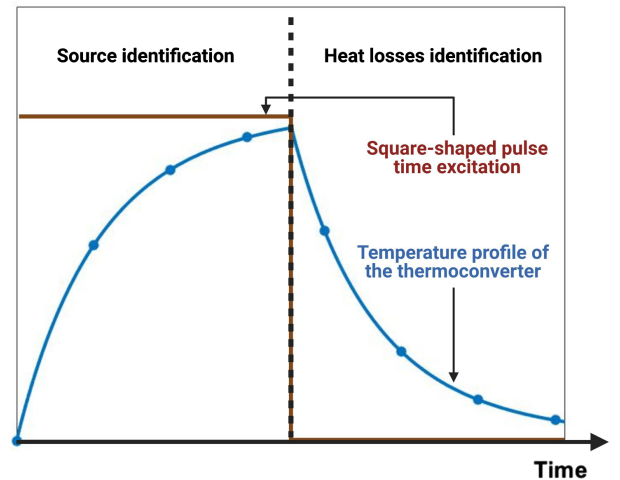


Fig. 6. Square-shaped pulse time excitation to be used for the estimation of the heat losses as well as the heat source.

Table 2. Thermophysical Properties of the Foam [32,33]

	Thickness (m)	λ ($\text{W m}^{-1} \text{K}^{-1}$)	ρC_p ($\text{J K}^{-1} \text{m}^{-3}$)	a ($\text{m}^2 \text{s}^{-1}$)
Foam	∞	0.03	47600	6.3×10^{-7}

$$h_{\text{estimated}} = \operatorname{argmin} \left\{ \left\| \bar{T}_{\text{model}}^*(t^*, h) - \bar{T}_{\text{mes}}^*(t^*) \right\|^2 \right\}. \quad (12)$$

C. Optimization of the Experimental Process for Estimation

To simultaneously and continuously estimate the convective heat loss and the excitation flux of the source, a square-shaped pulse is used for temporal excitation of the internal source. Figure 6 shows the square-shaped pulse time excitation as well as the temperature profile of the thermoconverter in the presence of the resulting heat losses. The choice of square-shaped pulse time excitation is justified by the fact that there is a constant level where the internal source is switched on (temperature rise of the thermoconverter), which is used to identify the source, and another constant level where the internal source is switched off (relaxation of the thermoconverter), which is used to estimate the heat loss. The estimation of the heat loss makes it possible to reintroduce this loss into the model described in Section 3.B and thus makes it complete.

5. RESULTS AND DISCUSSION

A. Contact Validation by Joule Effect

One of the most robust ways to control the power dissipated by a source is to use an electrical resistance heated by the Joule effect. This is used to validate the method of reconstruction of the source. To do this, a complex-shaped resistance with an internal ohmic resistance of 73Ω is used. The setup used is described in Fig. 7(a). An electrical current generator supplied the resistance during 1.5 s. The voltage is verified at the edge of the resistance by a voltmeter to be $U = 4.93$ V. This theoretically corresponds to the dissipation of a power equal to $P = 333$ mW. The thermoconverter is attached on the resistor, which is insulated by foam (polyurethane foam). Finally, an IR camera is used for the acquisitions.

In this case, only the parameters of the model to be used for the inversion are modified. The proposed model allows changing the parameters easily to match the real experimental configuration. One of the semi-infinite impedances of the air is then replaced by a semi-infinite impedance of the insulated foam, and the heat loss by convection is neglected on this side.

Figure 7(b) shows the normalized spatial average of the measured 3D temperature field. This field allows the identification of the t_0 and the construction of the new time base t^* , which is used to estimate the heat loss. Figure 7(c) shows the result of the minimization described in Section 4.B, and the convective exchange coefficient is estimated to be $4.53 \pm 0.3 \text{ W} \cdot \text{m}^{-2} \cdot \text{K}^{-1}$. The estimated value of this coefficient is coherent, given that one side of the thermoconverter is insulated by the foam, and the average increase in the temperature is low (on the order of 0.4 K at $t = 1$ s).

Figures 8(a) and 8(b) show the reconstruction of the spatial distribution and power density of the source after inversion.

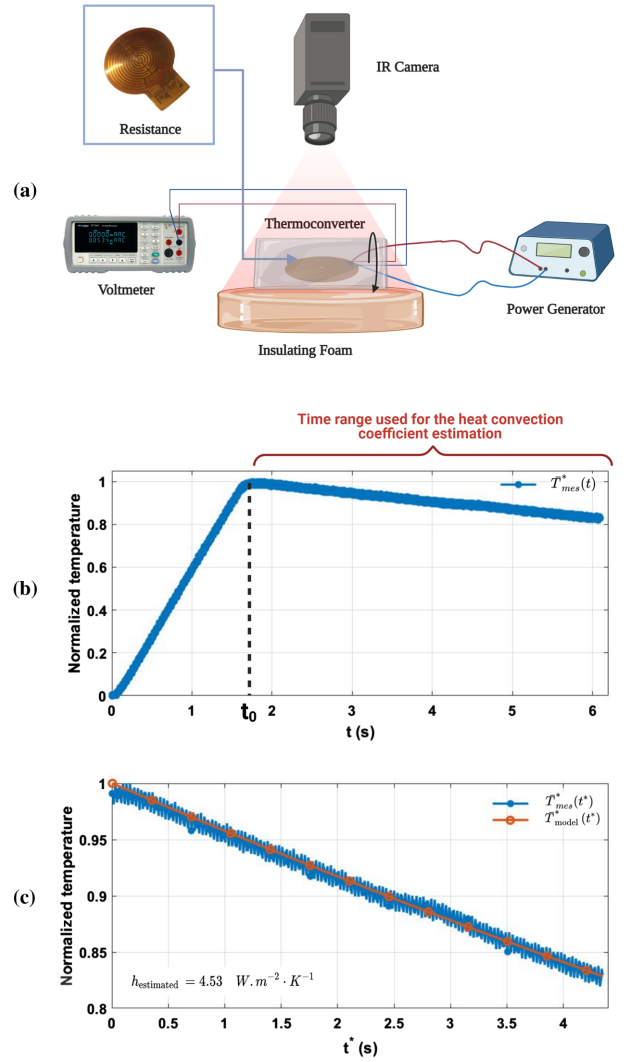


Fig. 7. (a) Experimental setup, (b) normalized spatial average of the 3D temperature field measured, and (c) comparison between the experimental data and the model using $h_c = 4.53 \text{ W} \cdot \text{m}^{-2} \cdot \text{K}^{-1}$.

It can be observed here that the spatial distribution of the estimated source fits well with the shape of the resistance presented in Fig. 7(a). Nevertheless, the spatial repartition of the flux is not uniform over the entire surface of the resistance, which can be explained by small adhesion defects between the thermoconverter and the resistance.

Figure 8(c) shows the reconstruction of the flux density for a single pixel over time. It can be seen that the flux density increases progressively (transient state) due to the inertia of the resistance (volumetric source) before reaching a constant level (steady state), which represents the real power density dissipated by the Joule effect.

Two methods exist to determine the injected flux: (i) multiplying the flux density imaged by the area and then integrating it or (ii) integrating the flux density image and multiplying the result by the area of one pixel. By applying the first method and considering that the absorbance of the thermoconverter in the IR is almost 100% [9], we obtain

$$P_{\text{estimated}} = \left(\oint \mathcal{Y}(x, y) \right) \times S_{\text{pixel}} = 331.5 \pm 1.9 \text{ mW}, \quad (13)$$

354
355
356
357
358
359
360
361
362
363
364
365
366
367
368
369
370
371

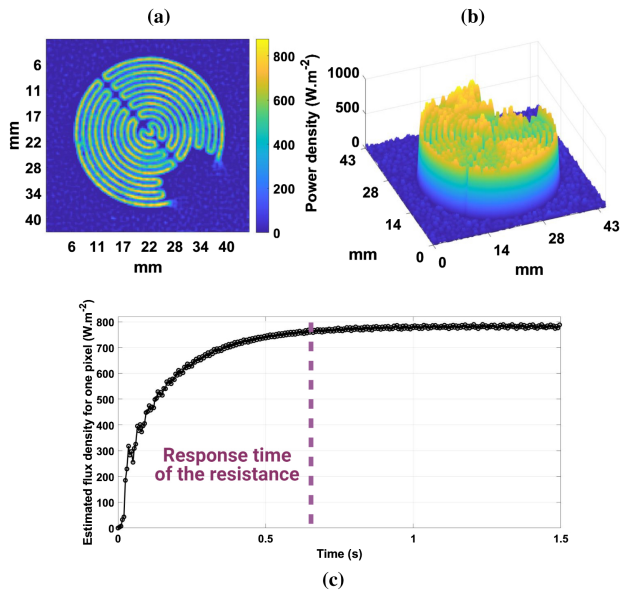


Fig. 8. (a) Image of the estimated source, (b) surface of the estimated source, and (c) estimated flux density for one pixel.

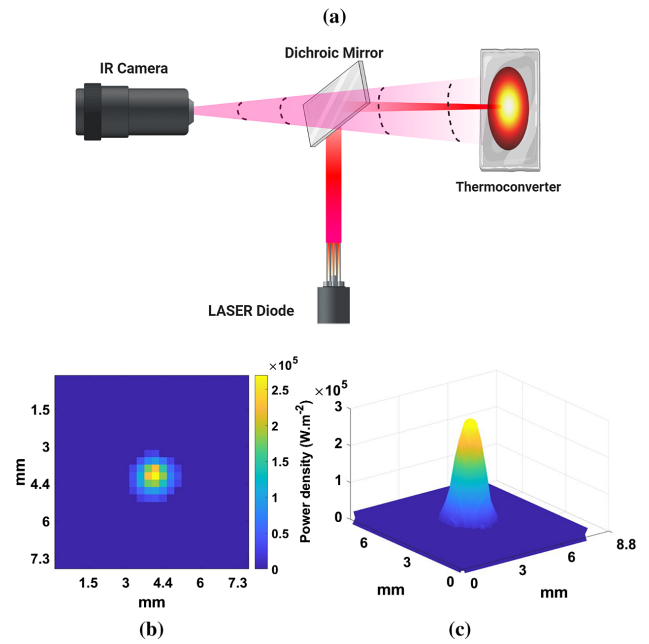


Fig. 9. (a) Experimental setup, (b) image of the estimated source, and (c) surface of the estimated source.

where S_{pixel} is the area of one pixel with a value of $8 \times 10^{-8} \text{ m}^2$. The estimation represents a relative error of 0.45%.

B. Contactless Application for Different Optical Sources

In this section, the use of our appliance as a power meter is demonstrated.

1. Near-IR Laser Source

In this first application, a NIR laser diode ($\lambda = 980 \text{ nm}$) with a power of $P = 280 \text{ mW}$ is used as an excitation source. The time of the square-shaped pulse is 40 ms. A dichroic mirror is placed between the IR camera and the thermoconverter, as shown in Fig. 9, and enabled to reach the temperature of the thermoconverter at the front side. As the thermoconverter is a thermally thin body, the temperature at the front side is equal to the temperature at the back side (no temperature gradient along the thermoconverter thickness). The thermoconverter is placed at a distance of 40 cm from the IR camera.

Figures 9(b) and 9(c) show the reconstruction of the spatial distribution and energy density of the source after inversion. The diameter of the spot after the flux estimation is equal to 3 mm, which is in agreement with the optical considerations. The estimated convective exchange coefficient is $h = 31 \text{ W} \cdot \text{m}^{-2} \cdot \text{K}^{-1}$. This value is very large compared to that estimated for the Joule heated resistance. This is due in small part to the fact that the thermoconverter is not insulated and in large part to the fact that the average temperature of the thermoconverter is very high (4 K at $t = 33 \text{ ms}$). The power estimated using Eq. (13) was found to be $285.3 \pm 3.7 \text{ mW}$ with a relative error of 1.9%.

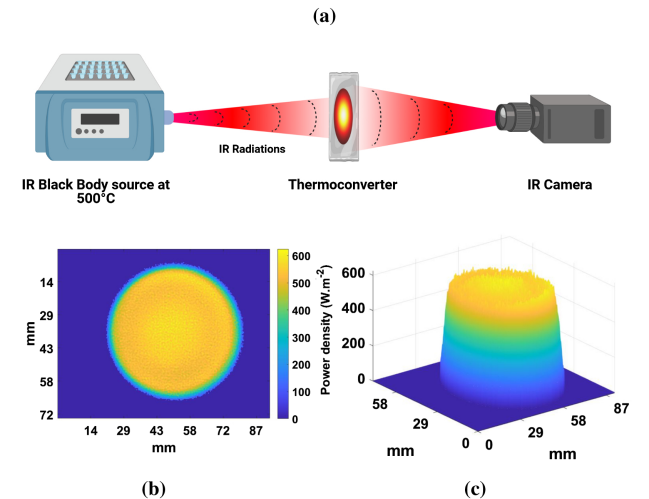


Fig. 10. (a) Experimental setup, (b) image of the estimated source, and (c) surface of the estimated source.

2. IR Blackbody Source

In this second application case, the source used comes from an IR blackbody (BBSH) from Prisma instruments, whose emissivity is estimated to have an uncertainty of 0.5% to $\epsilon_{\text{BB}} = 0.98$. The blackbody temperature is adjustable in the range [500°C; 1200°C]. In our case, the blackbody temperature is set to $T_{\text{BB}} = 500^\circ\text{C}$ [see Fig. 10(a)]. A square-shaped pulse of 4.5 s is applied using a chopper synchronized with the IR camera.

Figures 10(b) and 10(c) show the reconstruction of the spatial distribution and power density of the source after inversion. The thermoconverter is placed at a distance of 10 cm from the blackbody. The diameter of the blackbody nozzle is 43 mm. The spatial analysis of the estimated flux shows that the beam has a diameter of 60 mm, which represents a beam

401
402
403
404
405
406
407
408
409
410
411
412
413
414

415 divergence of 5° . The estimated convective exchange coefficient
 416 is $b = 17 \text{ W} \cdot \text{m}^{-2} \cdot \text{K}^{-1}$. This value is lower than that
 417 in the NIR laser case because the average temperature of the
 418 thermoconverter is also lower (2.5 K at $t = 1$ s).

419 The power estimated using Eq. (13) is $1.357 \pm 0.015 \text{ W}$. To
 420 validate the value of the estimated flux, a short calculation based
 421 on the Stefan–Boltzman law and the notion of the form factor
 422 in thermal radiation to allow modeling the radiative exchanges
 423 between two black disks ($\varepsilon \approx 1$) separated by a perfectly trans-
 424 parent medium is performed. This calculation predicts that
 425 the thermoconverter should theoretically receive a flux of
 426 $P = 1.15 \text{ W}$ and shows that the estimated flux is in the order of
 427 the magnitude of the expected power with a relative error equal
 428 to 15.25%.

429 3. Gigahertz Source

430 In this third application case, a Terasense gigahertz source
 431 ($f = 100 \text{ GHz}$, $\lambda = 3 \text{ mm}$) with a power of $P = 400 \text{ mW}$ is
 432 used, and the absorbance (\mathcal{A}) of the thermoconverter in this
 433 wave is equal to 61% [9]. The thermoconverter is placed at a
 434 distance of 5 cm from the source. The gigahertz source is syn-
 435 chronized with a waveform generator that allows delivery of a
 436 square-shaped pulse of 1.25 s.

437 The estimated convective exchange coefficient is
 438 $b = 20.24 \text{ W} \cdot \text{m}^{-2} \cdot \text{K}^{-1}$. This value is higher than that in
 439 the blackbody case and lower than that in the NIR laser case.
 440 This is related to the value of the average temperature of the
 441 thermoconverter, which is between those of the two cases (6 K
 442 at $t = 1$ s). Figures 11(b) and 11(c) show the reconstruction
 443 of the spatial distribution and power density of the source
 444 after inversion. In this case, the source power is estimated by
 445 modifying Eq. (13) to take into account the absorbance of the
 446 thermoconverter at the emission wavelength of the source as
 447 follows:

$$P_{\text{estimated}} = \left(\iint \mathcal{Y}(x, y) \right) \times S_{\text{pixel}} \times \frac{1}{\mathcal{A}}. \quad (14)$$

448 The power estimated using Eq. (14) is $404.8 \pm 5 \text{ mW}$ with a
 449 relative error equal to 1.19%.

450 4. Radio-Frequency Source

451 In this fourth application case, an ultra-high-frequency (UHF)
 452 radio wave antenna source ($f = 500 \text{ Mhz}$, $\lambda = 0.6 \text{ m}$) in an
 453 anechoic chamber is used. The thermoconverter used has a sur-
 454 face area of 1 m^2 , and it is placed at a distance of 1 cm from
 455 the source. The power delivered by the source and the absorbance
 456 of the thermoconverter at this wavelength are unknown, so the
 457 estimated flux is proportional to the absorbance of the thermo-
 458 converter. Figures 12(b) and 12(c) show the reconstruction of
 459 the spatial distribution and power density of the source after
 460 inversion. The estimated convective exchange coefficient is
 461 $b = 10.14 \text{ W} \cdot \text{m}^{-2} \cdot \text{K}^{-1}$. This value is the lowest of the con-
 462 vective exchange coefficient values estimated for the optical
 463 sources (except for the joule heat resistance). This is because the
 464 average temperature of the thermoconverter is lower than that
 465 in the previous cases [34] (1.3 K at $t = 1$ s). The power of the
 466 source estimated using Eq. (14) is $6.5 \pm 0.17 \times \frac{1}{\mathcal{A}} \text{ W}$. This

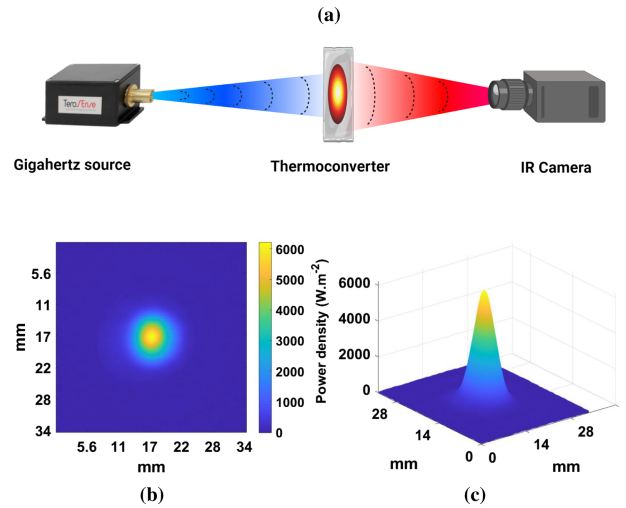


Fig. 11. (a) Experimental setup, (b) image of the estimated source, and (c) surface of the estimated source.

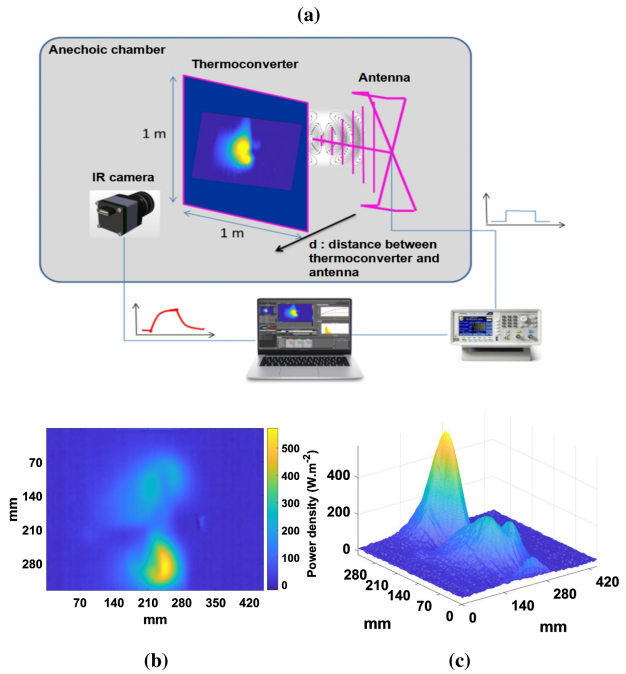


Fig. 12. (a) Experimental setup, (b) image of the estimated source, and (c) surface of the estimated source.

467 result is presented to demonstrate the hyperspectral aspect of the
 468 thermoconverter, on the one hand, and to highlight the need to
 469 know the absorbance of the thermoconverter (at the emission
 470 wavelength of the source) to estimate the power of the source, on
 471 the other hand.

472 C. Performances of the Sensor

473 The performances of the flux sensor are described here. It should
 474 be remembered that the sensor is the result of a coupled con-
 475 figuration thermoconverter-IR camera. Consequently, the
 476 performances of the sensor are linked and limited, on the one
 477 hand, by the characteristics of the camera ($25 \mu\text{m} \times 25 \mu\text{m}$)

Table 3. Performances of the Flux Sensor

	Joule Effect by Resistance	NIR Laser Source	IR Blackbody Source	Gigahertz Source	Radio-Frequency Source
Spatial resolution (μm^2)	283×283	180×180	290×290	280×280	1400×1400
sensitivity ($\mu\text{W}/\text{m}^2$)			$\frac{1.815 \times \text{TI}(\mu\text{s})}{A}$		

pitch size, minimum sensitivity of 20 mK, and variable according to the integration time), and, on the other hand, by the photothermal effect within the thermoconverter (absorbance, diffusion of the heat, and inversion of the heat transfer). The calculated spatial resolution varies depending on the sensor application due to the change in the thermoconverter-IR camera configuration in each case (size of the thermoconverter used, distance between the thermoconverter and the IR camera). The sensitivity of the sensor is given in the form of a general formula that takes into account the limits of the thermoconverter-IR camera configuration, the integration time of the camera, and the absorbance of the thermoconverter at the source wavelength.

6. CONCLUSION

A hyperspectral flux sensor using a thermoconverter to estimate the spatial distribution of a source and its flux density has been developed.

The most important point is the experimental validation of the thermoconverter and IR camera configuration. First, the development of a thermal model to precisely characterize the heat transfer within the thermoconverter was described. Then, a first inverse method was used to estimate the heat losses to increase the model's robustness and precision. Finally, a second inverse method allowed the spatial reconstruction of sources and their flux density.

The methodology was validated on a joule heated resistor, presented here as the reference. To illustrate the ultra-broadband quality of the technique, examples of applications with several sources have been discussed: (i) a NIR laser source, (ii) an IR blackbody source, (iii) a gigahertz source, and (iv) a UHF radio-frequency antenna.

This research offers new perspectives in the fields of hyperspectral fluxmetry and thermal inverse methods, with many applications projected in the fields of optical applications, building science, and industries.

Funding. Centre National de la Recherche Scientifique.

Acknowledgment. This research is part of the IGAR project that aims to thermally and chemically characterize plasma torches. The main challenge is the non-contact 3D temperature and flux field measurement for energy optimization of these torches. The authors thank ADEME for the support of this work through the IGAR project with Arcelor-Mittal.

Disclosures. The authors declare no conflicts of interest.

Data Availability. Data underlying the results presented in this paper are not publicly available at this time but may be obtained from the authors upon reasonable request.

REFERENCES

1. D. Jaeggi, H. Baltés, and D. Moser, "Thermoelectric ac power sensor by CMOS technology," *IEEE Electron Device Lett.* **13**, 366–368 (1992).

2. J. C. Johnson and G. A. Massey, "Bolometric laser power meter for sensitive measurements in the IR–vacuum UV spectral range," *Appl. Opt.* **17**, 2268–2269 (1978).
3. G. E. Mohler, "Laser power meter," (1975).
4. G. A. Rex, "Laser power-energy meter," (1971).
5. C. Pradere, J. Caumes, D. Balageas, S. Salort, E. Abraham, B. Chassagne, and J. Batsale, "Photothermal converters for quantitative 2D and 3D real-time terahertz imaging," *Quant. InfraRed Thermogr. J.* **7**, 217–235 (2010).
6. R. Müller, W. Bohmeyer, M. Kehrt, K. Lange, C. Monte, and A. Steiger, "Novel detectors for traceable THz power measurements," *J. Infrared Millim. Terahertz Waves* **35**, 659–670 (2014).
7. W. Flores-Fuentes, J. E. Miranda-Vega, M. Rivas-López, O. Sergiyenko, J. C. Rodríguez-Quiñonez, and L. Lindner, "Comparison between different types of sensors used in the real operational environment based on optical scanning system," *Sensors* **18**, 1684 (2018).
8. D. L. Balageas, P. Levesque, and A. A. Deom, "Characterization of electromagnetic fields using a lock-in infrared thermographic system," *Proc. SPIE* **1933**, 274–285 (1993).
9. M. Romano, A. Chulkov, A. Sommier, D. Balageas, V. Vavilov, J. Batsale, and C. Pradere, "Broadband sub-terahertz camera based on photothermal conversion and IR thermography," *J. Infrared Millim. Terahertz Waves* **37**, 448–461 (2016).
10. H. Gidik, D. Dupont, and G. Bedek, "Development of a radiative heat fluxmeter with a textile substrate," *Sens. Actuators A* **271**, 162–167 (2018).
11. C. Jim and H. He, "Estimating heat flux transmission of vertical greenery ecosystem," *Ecol. Eng.* **37**, 1112–1122 (2011).
12. K. Yang and J. Wang, "A temperature prediction-correction method for estimating surface soil heat flux from soil temperature and moisture data," *Sci. China D* **51**, 721–729 (2008).
13. J. Gardarein, J. Battaglia, S. Lohle, P. Jullien, B. Van Ootegem, J. Couzi, and J. Lasserre, "Miniaturized heat flux sensor for high enthalpy plasma flow characterization," *Inverse Probl. Sci. Eng.* **21**, 1–14 (2013).
14. A. Zribi, M. Barthès, S. Bégot, F. Lanzetta, J. Rauch, and V. Moutarlier, "Design, fabrication and characterization of thin film resistances for heat flux sensing application," *Sens. Actuators A* **245**, 26–39 (2016).
15. M. Groz, E. Abisset-Chavanne, A. Meziane, A. Sommier, and C. Pradere, "Bayesian inference for 3D volumetric heat sources reconstruction from surfacic IR imaging," *Appl. Sci.* **10**, 1607 (2020).
16. M. Groz, E. Abisset-Chavanne, A. Meziane, A. Sommier, and C. Pradere, "Three-dimensional reconstruction of thermal volumetric sources from surface temperature fields measured by infrared thermography," *Appl. Sci.* **9**, 5464 (2019).
17. P. Burgholzer, M. Thor, J. Gruber, and G. Mayr, "Three-dimensional thermographic imaging using a virtual wave concept," *J. Appl. Phys.* **121**, 105102 (2017).
18. S. Waters, P. Burgholzer, A. Mendioroz, and I. S. de Ocariz, "3D reconstruction of tilted cracks using infrared thermography and the virtual wave concept," *14th International Conference on Quantitative Infrared Thermography*, Berlin, Germany (2018), pp. 25–29.
19. D. Nortershauser and P. Millan, "Resolution of a three-dimensional unsteady inverse problem by sequential method using parameter reduction and infrared thermography measurements," *Numer. Heat Transfer* **37**, 587–611 (2000).
20. D. Nortershauser and P. Millan, "Estimation of moving heat sources with a three-dimensional unsteady inverse method," *Aerosp. Sci. Technol.* **5**, 529–540 (2001).
21. E. Badine, M. Bardoux, N. Abboud, M. Depriester, S. Longuemart, Z. Herro, and A. H. Sahraoui, "Thermorefectance profile analysis and multiparameter 3D fitting model applied to the measurement

- 589 of thermal parameters of thin film materials," *J. Phys. D* **52**, 205303
590 (2019). 609
- 591 22. D. Maillet, S. André, J.-C. Batsale, A. Degiovanni, and C. Moyne, 610
592 *Thermal Quadrupoles, Solving the Heat Equation Through Integral* 611
593 *Transforms* (Wiley-Blackwell, 2000). 612
- 594 23. J. Pailhes, C. Pradere, J.-L. Battaglia, J. Toutain, A. Kusiak, A. W. 613
595 Aregba, and J.-C. Batsale, "Thermal quadrupole method with internal 614
596 heat sources," *Int. J. Thermal Sci.* **53**, 49–55 (2012). 615
- 597 24. J. Toutain, J. Battaglia, C. Pradere, J. Pailhes, A. Kusiak, W. Aregba, 616
598 and J. Batsale, "Numerical inversion of Laplace transform for time 617
599 resolved thermal characterization experiment," *J. Heat Transfer* **133**, 618
600 044504 (2011). 619
- 601 25. L. Gaverina, J. Batsale, A. Sommier, and C. Pradere, "Pulsed flying 620
602 spot with the logarithmic parabolas method for the estimation of 621
603 in-plane thermal diffusivity fields on heterogeneous and anisotropic 622
604 materials," *J. Appl. Phys.* **121**, 115105 (2017). 623
- 605 26. F. White, *Heat and Mass Transfer*, Series in Mechanical Engineering 624
606 (Addison-Wesley, 1988). 625
- 607 27. J. Hadamard, *Lectures on Cauchy's Problem in Linear Partial* 626
608 *Differential Equations* (Yale University, 1923).
28. A. Tikhonov, "On the solution of ill-posed problems and the method 609
of regularization," *Russ. Acad. Sci.* **151**, 501–504 (1963). 610
29. R. Gray, "Toeplitz and circulant matrices: a review," *Found. Trends* 611
Commun. Inf. Theory **2**, 155–239 (2006). 612
30. E. Picard, "Sur un theoreme general relatif aux equations integrales 613
de premiere espece et sur quelques problemes de physique mathe- 614
matique," *Rend. Circ. Mate. Palermo* **29**, 79–97 (2010). 615
31. J. A. Nelder and R. Mead, "A simplex method for function minimiza- 616
tion," *Comput. J.* **7**, 308–313 (1965). 617
32. N. S. Bondareva, M. Sheikholeslami, and M. A. Sheremet, "The influ- 618
ence of external temperature and convective heat exchange with an 619
environment on heat transfer inside phase change material embed- 620
ded brick," *J. Energy Storage* **33**, 102087 (2021). 621
33. E. Placido, M. Arduini-Schuster, and J. Kuhn, "Thermal properties 622
predictive model for insulating foams," *Infrared Phys. Technol.* **46**, 623
219–231 (2005). 624
34. J.-W. Wu, W.-F. Sung, and H.-S. Chu, "Thermal conductivity of poly- 625
urethane foams," *Int. J. Heat Mass Transfer* **42**, 2211–2217 (1999). 626